Journal of Colloid and Interface Science 700 (2025) 138344

Contents lists available at ScienceDirect

Journal of Colloid And Interface Science

journal homepage: www.elsevier.com/locate/jcis

Droplet confined binary colloidal co-assembly into hierarchical Supraparticles with controllable morphology

Huan Liu [a,1], Shijian Huang [a,1], Zhenping Liu [b], Lang Chen [a], Jiamei Chen [b,c], Xinyi Li [a], Mengjun Liu [a], Haoqiang Feng [b], Weilong Xu [b], Ruizhi Yang [d], Minmin Zhang [a], Lingling Shui [a,*]

[a] Guangdong Provincial Key Laboratory of Nanophotonic Functional Materials and Devices, Guangdong Basic Research Center of Excellence for Structure and Fundamental Interactions of Matter, School of Optoelectronic Science and Engineering, South China Normal University, Guangzhou 510006, China
[b] International Joint Laboratory of Optofluidic Technology and System (LOTS), National Center for International Research on Green Optoelectronics, South China Academy of Advanced Optoelectronics, South China Normal University, Guangzhou 510006, China
[c] Department of Pharmacy, Shenzhen Bao'an Traditional Chinese Medicine Hospital, Guangzhou University of Chinese Medicine, Shenzhen 518133, China
[d] Soft Condensed Matter, Debye Institute for Nanomaterials Science, Utrecht University, Princetonplein 1, 3584 CC, Utrecht, the Netherlands

GRAPHICAL ABSTRACT

Emulsion droplet confined co-assembly of PS and CNT binary soft colloids allows control over both chemical and physical conditions to construct hierarchical supraparticles. The morphologies and detailed structures can be modulated via the colloidal size, the ratio of binary particles, the solvent removal speed, and assembly speed induced phase separation.

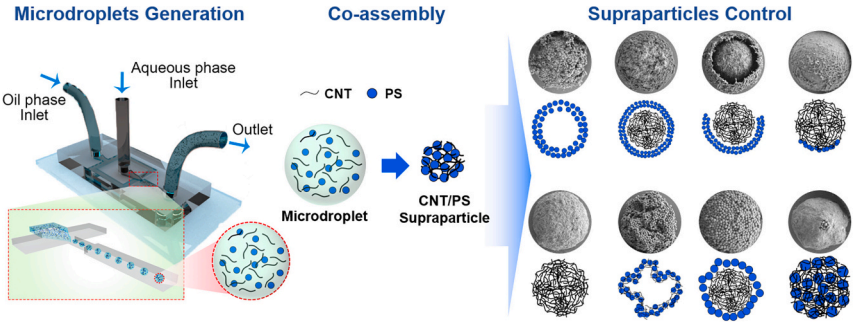

ARTICLE INFO

Keywords:
Co-assembly
Microfluidics
Supraparticles
Carbon nanotubes
Polystyrene

ABSTRACT

Physically confined assembly of binary colloidal mixtures in emulsion droplets provides a versatile platform for engineering supraparticles with tunable morphologies and functionalities. While single-component and hard-sphere colloidal assemblies have been extensively studied, the co-assembly of binary soft colloids presents unresolved challenges in architecture control and functional integration. In this work, we investigate the *co*-assembly performance of emulsion droplet confined binary soft colloids of spherical polystyrene nanoparticles (PS) and wire-like carbon nanotubes (CNTs). The supraparticles of CNT/PS with various architectures have been obtained by varying the solvent removal dynamics and the binary colloidal composition. We find out that the binary colloidal size and mass ratio govern the CNT/PS supraparticle structural diversity, ranging from core-shell, core-semishell, garnet-like to densely packed architectures. Spontaneous emulsification and microphase

* Corresponding authors at: Joint Laboratory of Optofluidic Technology and Systems (LOTS), National Center for International Research on Green Optoelectronics, School of Optoelectronic Science and Engineering, South China Normal University, Guangzhou 510006, China.
E-mail address: shuill@m.scnu.edu.cn (L. Shui).
[1] These authors contributed equally to this work.

https://doi.org/10.1016/j.jcis.2025.138344
Received 20 April 2025; Received in revised form 30 June 2025; Accepted 2 July 2025
Available online 3 July 2025

segregation drive the transformation from core-shell to core-semishell architectures, revealing the critical role of fluid dynamics and confinement effects. This understanding of mechanism enables the rational design of hybrid magnetic supraparticles, demonstrating the broad applicability of such an approach. By establishing clear composition-structure correlations, this work advances the controlled co-assembly of binary colloids into hierarchical supraparticles, offering a pathway for constructing functional materials with tailored complexity.

1. Introduction

Supraparticles, a rapidly developing class of nano- to microscale particles ranging from a few to hundreds of microns, bridge the gap between nanoscale synthesis and macroscale processing. The tunable properties, determined by chemical composition and physical structure, enable them to be highly potential for various applications [1,2]. These hierarchically structured supraparticles exhibit distinctive features such as enhanced accessibility, high porosity, and expansive surface area [3], allowing them to be applied in optics [4–6], sensing [7,8], catalysis [9,10], and energy [11,12]. The construction of supraparticles typically follows two strategies [13]: the thermodynamics/kinetics-driven assembly which leverages weak interactions including hydrogen bonding and hydrophobic forces; and the template-controlled assembly which employs templates to confine and induce assembly via physicochemical forces such as capillary action and van der Waals forces. Among these, the utilization of droplets as soft templates for colloidal encapsulation and confinement, followed by solvent evaporation, stands out as a facile and versatile method, holding potential for advancements in supraparticle preparation [14].

Droplet generation, an essential step in the assembly process, can be achieved through various methods, such as vortex oscillation [15], spray-drying [16], membrane separation [17], and microfluidics [18–20]. Microfluidics is particularly advantageous for producing monodisperse droplets with high uniformity, which is essential for confined assembly studies and the precise construction of supraparticles. In contrast to spray-drying or direct drying on superhydrophobic surfaces, microfluidic emulsions necessitate solvent removal through the continuous phase, leading to relative slow drying kinetics. Such a slower process on the other hand enhances the structural diversity and stability of the resulting supraparticle assemblies, contributing to their improved properties [21,22].

Recent research on colloidal assembly within emulsions has focused primarily on simulating atomic-scale organization, understanding the principles and governing law of self-assembly, and exploring the unique properties of supraparticles [23,24]. Studies have predominantly utilized single-component colloids, such as polystyrene nanoparticles (PS) [25], silicon nanoparticles (SiO_2) [26], and cobalt iron oxide nanoparticles ($CoFeO_x$) [27], to mimic hard sphere systems. The advanced materials, including metal-organic framework nanoparticles (MOF) [28], covalent organic framework nanoparticles (COF) [29], and lanthanide fluoride (LnF_3) [30] have been employed to construct novel supraparticles. Although binary supraparticles have been successfully constructed [9,31,32], the assembly dynamics of binary colloidal nanoparticles in emulsions are more complex compared to the single colloidal particles, particularly in non-hard sphere systems. This complexity underscores the need for deep insights into heterogeneous self-assembly in confined emulsions, being critical for developing diverse supraparticle structures and their applications.

Herein, a binary mixture of polystyrene nanoparticles (PS) (contributing to form shells in supraparticles) and carbon nanotubes (CNT) (contributing to form cores in supraparticles) was confined in emulsion droplets prepared using microfluidic devices. The resulting CNT/PS hybrid supraparticles exhibited a serial of structural configurations beyond the simple core-shell design, including shell-like, core-semishell, garnet-like, and densely packed appearances (Fig. 1). These structural variations are influenced by the PS nanoparticle size and the mass ratio of CNT to PS. Through the systematic investigation, we have explored how the supraparticle architectures were affected by these factors, suggesting the importance of both interparticle interactions and the kinetics of solvent removal. In the water-in-hexadecane emulsion system, where sorbitan monooleate (commercially termed Span 80) acted as a surfactant, the transport/removal of water from droplets was facilitated by the surfactant-assisted spontaneous emulsification. By adjusting the concentration of Span 80 (10–30 wt%) and temperature (25–60 °C), we regulated the rate of spontaneous emulsification, thereby manipulating the kinetics of water removal from the droplets. This tuning strategy provides valuable insights into the mechanism underlying the architecture transition of supraptaicles from core-shell microcapsule/microsphere to core-semishell microsphere, revealing the sensitivity of the self-assembly dynamics to external factors. Furthermore, this strategy of emulsion confinement and structure tuning has been successfully applied to construct magnetic supraparticles using a binary colloidal mixture of PS and CNT@Fe_3O_4.

2. Materials and methods

2.1. Materials

Polystyrene nanoparticles (PS NPs, 50 mg/mL) aqueous dispersion was purchased from Huge Biotechnology Co., Ltd. (Shanghai, China). The multi-walled carbon nanotube (MWCNTs, outer diameter 20–30 nm, length 10–20 μm, >95 % purity) was ordered from DKnano Co., Ltd. (Beijing, China). The iron(III) acetylacetonate ($Fe(acac)_3$, 98 % purity triethylene glycol (TEG, 98 % purity) n-hexadecane (98 % purity) and the sorbitan monooleate (Span 80, Analytical reagent (AR) grade) were purchased from Aladdin Reagents Co., Ltd. (Shanghai, China). Hydrochloric acid (HCl), Sulfuric acid (H_2SO_4), Nitric acid (HNO_3) (AR grade) and ethanol (≥99.7 % purity) were all ordered from Guangzhou chemical reagent Co., Ltd. (Guangdong, China). All chemical reagents were used as received without further purification. Deionized (DI) water with a resistivity of ≥18.25 MΩ·cm was prepared using the Milli-Q water purification system (Water Purifier Co., Ltd., Sichuan, China).

2.2. Characterization methods

The droplet generation process was monitored by using an optical microscope (GX53, Olympus, Japan) equipped with a high-speed camera (Phantom MIRO M110, Vision Research, USA). Optical images were captured with a BX53 Olympus microscope, utilizing both reflected and transmitted light in conjunction with a DP28 camera. For structure characterization of the supraparticles, a suspension of the prepared particles in ethanol was deposited onto a clean silicon substrate and allowed to dry naturally at room temperature. The detailed structure of these supraparticles was characterized using a FEI-SEM (ZEISS ultra 55, Carl Zeiss, Germany) with an accelerating voltage of 2–10 kV. The contact angle (θ) was measured using an OCA pro 15 (Dataphysics, Germany) and the zeta potential (ζ) was determined using a Nano plus 3 (Micromeritics, USA). Viscosity measurements were performed using a rheometer (HAAKE MAR III, Thermo Fisher Scientific Inc., USA). Transmission electron microscope (TEM) images of CNT@Fe_3O_4 were captured on a Tecnai G2 F30 electron microscope under an accelerating voltage of 300 keV. Magnetization curves were measured using a Vibrating Sample Magnetometer (VSM, LakeShore 8604, USA) at 300 K, with the magnetic field range set to ±20,000 Oe.

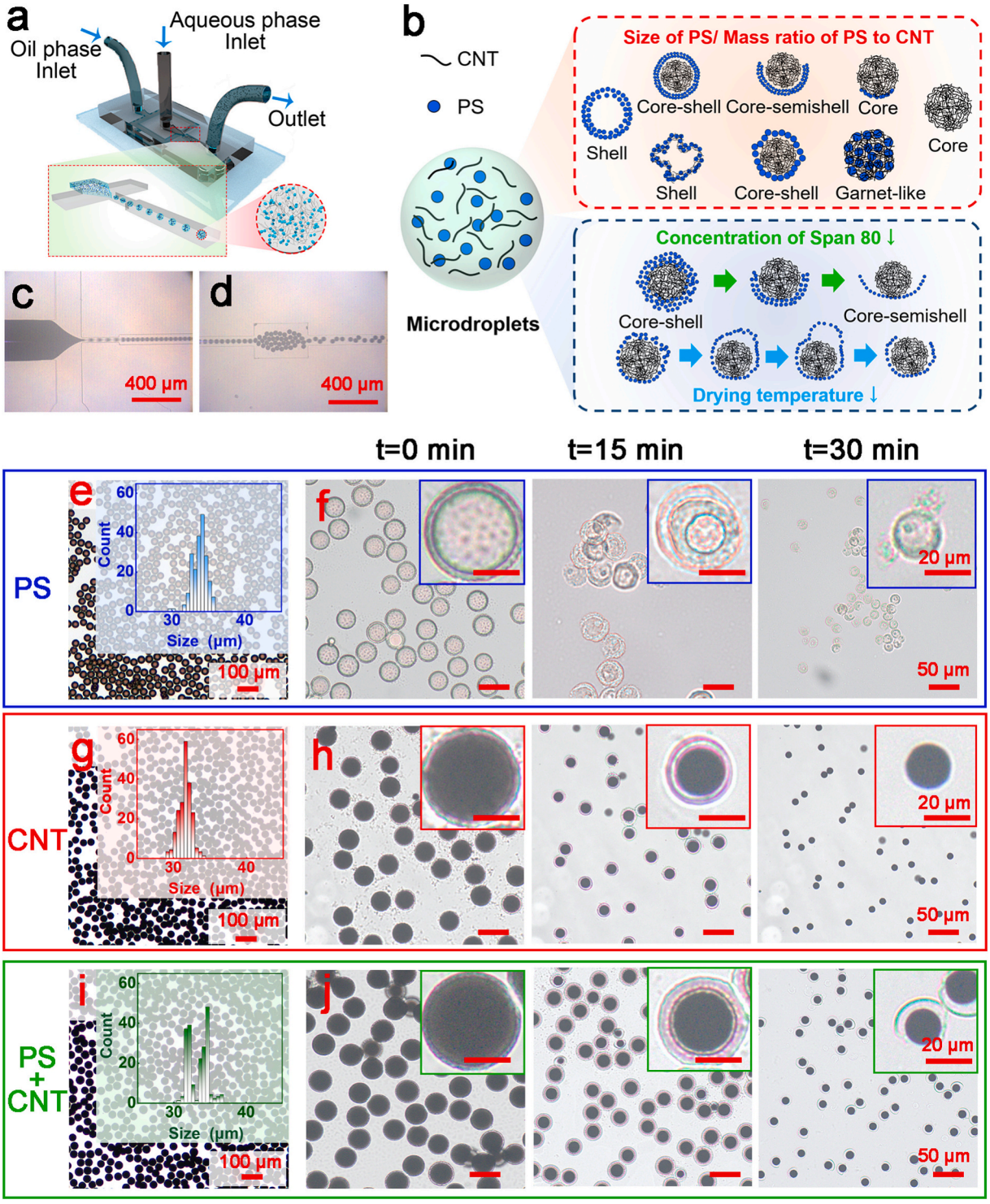

Fig. 1. (**a**) Schematic of the microfluidic device for droplet preparation. (**b**) Drawings showing the representative structures of droplet confined CNT/PS hybrid supraparticles. Optical images of (**c**) droplet generation at the flow-focusing junction and (**d**) the obtained droplets at the downstream area with a puffer reservoir. Optical images of the as-prepared droplets with the inner phases of (**e, f**) PS dispersion, (**g, h**) CNT dispersion, and (**i, j**) PS and CNT blend dispersion, respectively. The insets show the corresponding size distribution and demonstrate the gradual shrinkage of the microdroplets over time.

2.3. Acid-oxidation treatment for MWCNTs

To enhance the dispersibility of MWCNTs in water, a covalent modification method was conducted [33]. 3.0 g MWCNTs were added into 300 mL acid mixture of HNO_3 and H_2SO_4 with volume ratio of 1:3 (V/V) in a round-bottomed flask. The flask was placed in an oil bath and heated at 50 °C for 12 h. After the reaction, the product was collected via centrifugation at 7000 rpm and thoroughly washed with DI water. Subsequently, the resulting precipitate was dialyzed in a dialysis bag with molecular weight cutoff of 3500 Da against DI water for 48 h to remove remain ions. The dispersion was then freeze-dried for 24 h to obtain carboxyl-functionalized MWCNT (MWCNT-COOH). Unless otherwise stated, all CNTs referenced in this study are MWCNT-COOH.

2.4. Synthesis of CNT@Fe_3O_4 nanohybrids

CNT@Fe_3O_4 nanohybrids (CNT@Fe_3O_4) were synthesized according to the previously reported work [34]. Briefly, 400 mg $Fe(acac)_3$ and 100 mg CNTs were dispersed in 60 mL TEG solution. The mixture was then heated at 200 °C for 12 h for reaction. Afterwards, the product was centrifuged and washed three times sequentially with ethanol and water. The obtained CNT@Fe_3O_4 nanohybrids were then magnetically separated and dried in a vacuum oven.

2.5. Preparation of dispersions used as inner phase

The aqueous dispersions containing colloidal particles were used as the inner phase which became droplets using a microfluidic device. The inner phases were prepared using CNT (10 mg/mL), CNT/Fe_3O_4 (10 mg/mL) and PS (10 mg/mL) dispersions. As a prime example, the mixed dispersion with a 1:1 mass ratio of CNT to PS was prepared by adding 1 mL CNT dispersion (10 mg/mL) and 1 mL PS dispersion (10 mg/mL) into a centrifuge tube, diluting with DI water to a final solid content of 5 mg/mL, and sonicating for 6 h. Mixed dispersions with other CNT-to-PS mass ratios were prepared using the same procedure.

2.6. Construction of supraparticles

Polydimethylsiloxane (PDMS) microfluidic droplet generators with flow-focusing geometries were fabricated via soft lithography. The channels for droplet generation was designed with both width and depth of 50 μm (**Fig. S1a, b**). The continuous (outer) and dispersed (inner) phases were delivered to the microfluidic device using syringe pumps (LSPO2-1B, Longer, Hebei, China). Syringes were connected to the device using flexible silicone tubing (outer diameter of 1.5 mm, inner diameter of 0.5 mm). The flow rates of the outer phase were intentionally set to 15 μL/min (for a continuous phase consisting of 5 wt% Span 80 hexadecane solution), 13 μL/min (with a 10 wt% Span 80 hexadecane solution),10 μL/min (with a 20 wt% Span 80 hexadecane solution), 7 μL/min (utilizing a 30 wt% Span 80 hexadecane solution) with the inner phase flow rate fixed at 2 μL/min. This flow configuration was designed to achieve incrementally varying matrix compositions while maintaining consistent droplet diameter of ~35 μm across different surfactant concentrations. During droplet generation, the droplets were collected in a cell culture dish (plastic, 90 × 20 mm) containing 2 mL outer phase.

The dishes were dried in an oven for 24 h to evaporate water from droplets. To investigate the effect of temperature on droplet shrinkage kinetics, droplets were dried in the oven for 24 h at different temperatures (25 °C, 30 °C, 40 °C, 50 °C and 60 °C). As the moisture within the droplets was depleted via controlled evaporation, the solute components underwent a sophisticated self-assembly process, resulting in the formation of supraparticles with unique morphologies and detailed architectures. The risk of supraparticle fragmentation or abscission of PS should be minimized in subsequent washing and observation steps. To maintain the integrity of the formed structure, the supraparticles were treated at 85 °C for 5 min after assembly. Thereafter, the supraparticles were separated from the oil phase by centrifuging at a speed of 10,000 rpm for 1 min using a centrifuge (MTX-125, Thermo Fisher Scientific Inc. China) and then washed three times with ethanol. Finally, the supraparticles were dried in a 1 mL centrifuge tube at room temperature.

2.7. Measurement of droplet solidification rate

Time-series images were taken after the stable droplet generation. Droplet diameters were quantified using CellSens software. To estimate the solidification rates of large batches of droplets, the emulsions were produced to cover approximately half of the surface area of a culture dish. Droplets sank down in the emulsion on the surface of coverslip due to the density difference. The center region of the emulsion was selected for video recording, and the average diameter was measured from 50 randomly selected droplets for each time point. A temperature controlling stage (LTS120/PE100/PE120, Linkam Scientific Instruments, England) was used to maintain the temperature for droplet diameter measurements at different temperatures (25 °C, 30 °C, 40 °C, 50 °C and 60 °C). Mean size of droplets was presented as the number mean and standard deviation. Droplet shrinkage rate was calculated as the ratio of the real time droplet diameter (D_t) to the initial droplet diameter (D_0).

3. Results and discussion

3.1. Monodispersed droplet generation via microfluidics

Fig. 1a illustrates the emulsion droplet preparation via a flow-focusing microfluidic device. The inner phase (aqueous phase) is sheared into microdroplets by the outer phase (oil phase) at the junction of the flow-focusing polydimethylsiloxane (PDMS) microfluidic chip (as shown in Fig. 1c). The microchannels at the junction area is 45.3 μm deep and 51.8 μm wide (**Fig. S1a, b**). Hexadecane, containing non-ionic surfactant Span 80, was utilized as the outer phase to stabilize the water-in-oil (W/O) emulsion droplets (Fig. 1d). Due to the density difference, the collected droplets rapidly sediment to the bottom of the vessel, where they solidify into microspheres as the particles assemble with the evaporation of solvent [35].

The emulsion (approximately 500 droplets in 200 μL oil phase) was collected using a hydrophobic plastic dish and placed under an optical microscope to record the transformation process from droplets to microparticles (supraparticles) at room temperature. The homogeneous aqueous dispersion containing PS (100 nm, 5 mg/mL), CNT (5 mg/mL) and their blend was emulsified into droplets (templates for particle assembly), with average diameters of 33 ± 3 μm (n = 200, the coefficient of variation (CV) = 2.84 %), 32 ± 2 μm (n = 200, CV = 2.73 %) and 33 ± 2 μm (n = 200, CV = 4.03 %), respectively, as illustrated in **Figs. 1e**, **g** and **i**. It is worth noting that the oil phase used here was hexadecane containing 20 wt% Span 80 (the critical micelle concentration of Span 80 in hexadecane, ~0.007 wt%), which effectively stabilized the emulsion droplets during drying, especially those containing PS (**Fig. S2**). The water removal from the microdroplets occurs through evaporation and the spontaneous emulsification due to the existence of Span 80 which transfers water from the droplets to the outer phase in the form of reverse micelles [36,37]. A shell formation was observed on the droplet surface, with the droplet volume shrinking by half within 15 min. In 30 min, the colloid particles assembled into solid microparticles (supraparticles), with the composition being clearly observed via the optical microscopy in transmission mode, where PS and CNT are transparent and black, respectively, as shown in **Figs. 1f, h** and **j**.

As the solvent evaporated and the colloidal particles assembled under the spherical confinement provided by the droplet templates, the inherent hydrophobic and electrostatic interactions of the materials influenced their organization. PS NPs (water contact angle θ_w of 66.5 ± 0.5°, zeta potential ζ of −71 ± 3 mV, shown in **Fig. S3a**, **b**) preferentially assembled at the water-oil interface, leading to the formation of a shell (Fig. 1f). CNT (θ_w = 12.8 ± 1.0°, ζ = 53 ± 7 mV, shown in **Fig. S3a**, **b**) aggregated into a solid and dense core (Fig. 1h). However, when the microparticles were formed from the PS and CNT blend dispersion, the obtained supraparticle exhibited a core-semishell configuration, rather than a conventional core-shell structure (Fig. 1j). This highlights the complexity of binary colloidal co-assembly and the challenges in controlling the formed supraparticle structures.

3.2. Tunable morphologies of CNT/PS hybrid supraparticles

The prepared emulsion droplet provides a uniform template with a micro-scale medium confined by a soft liquid interface, which prevents colloids from escaping while allowing molecular transport and solvent exchange, ideally for confined particle assemble to construct versatile

architectures [38]. Herein, we investigated the co-assembly behavior of PS and CNT within the W/O emulsion droplet system.

To create binary colloidal dispersions, PS and CNT dispersions were mixed at different ratios and emulsified into droplets with diameters of ~35 μm via the microfluidic devices (**Fig. S4**). Hexadecane containing 20 wt% Span 80 was used as the continuous (outer) phase. The microdroplets were collected in a hydrophobic plastic dish and placed at 25 °C until all the droplets dried into supraparticles. Despite the formation of supraparticles in the oil phase, the formed structure was unstable and easily fragmented during washing and transferring. Therefore, to stabilize the obtained structures, the microparticles (in outer phase) were at 80 °C for 5 min. This mild heating caused the PS particles to slightly melt and fuse together, allowing the microparticles to separate from the oil phase and maintain their structure when observed under an optical microscopy in transmission mode. As displayed in Fig. 2, all microparticles retained a relatively spherical shape, attributed to the effective confinement provided by the droplet template.

The obtained supraparticles were placed on a silicon wafer and observed under an optical microscope in reflectance mode, PS microcapsules appeared in white (Fig. 2a), while the CNT microspheres appeared in black (Fig. 2c). SEM images further confirmed the formation of PS microcapsules (Fig. 2b) and CNT microspheres (Fig. 2d), with an average diameter of 12 ± 2 μm and 10 ± 1 μm, respectively. From the morphological perspective, the PS microcapsules exhibit a disordered structure (Fig. 2b), whereas the CNT microspheres present a smooth surface (Fig. 2c). This difference can be primarily attributed to the distinct assembly mechanisms of PS and CNT within the emulsion droplets. PS NPs, being spherical and isotropic with negative surface charges, tend to adsorb at the oil-water interface and form a core-shell microcapsule. In contrast, CNTs, with their high aspect ratio and tendency to align along the direction of applied forces, form a solid microsphere with relatively smooth surface when assembled within the W/O droplet template under the proposed experimental conditions. SEM images of the crushed supraparticles verified the formation of hollow microspheres (microcapsules) with PS shells (**Fig. S5a**) and solid CNT cores (**Fig. S5b**), as observed in the transmission mode (PS shell in **Fig. S4a** and CNT core in **Fig. S4e**).

Under the constant experimental conditions, we observed that the structure of CNT/PS supraparticles were highly dependent on the PS particle size (denoted as d_{PS}) and the PS to CNT ratio (denoted as $R_{PS:\ CNT}$). A well-defined core-shell structure with a PS shell and CNT core was obtained at d_{PS} = 100 nm and $R_{PS:\ CNT}$ = 3:1. The architectures were clearly resolved under reflection mode of the microscope (Fig. 2e), being consistent to the image obtained under transmission mode (**Fig. S4b**). SEM characterization further confirmed the smooth and continuous surface structure of the PS shell (Fig. 2f). When $R_{PS:\ CNT}$ was reduced to 1:1 at d_{PS} = 100 nm, the supraparticles changed to a core-semishell architecture with PS forming a partial shell around the CNT core (Fig. 2g). Both optical and SEM images demonstrate that the formed structures remained intact through washing and transfer processes (Fig. 2g, h; **Fig. S4c**), indicating their remarkable mechanical stability. Moreover, the quantitative analysis of size distribution (**Fig. S6**) revealed exceptional uniformity across all architectures, with the size CV <5 %. Further decreasing $R_{PS:\ CNT}$ to 1:3 produced supraparticles with a dominant CNT core and a tiny PS cap (Fig. 2i, j; **Fig. S4d**), demonstrating the potential control of supraparticle structure through

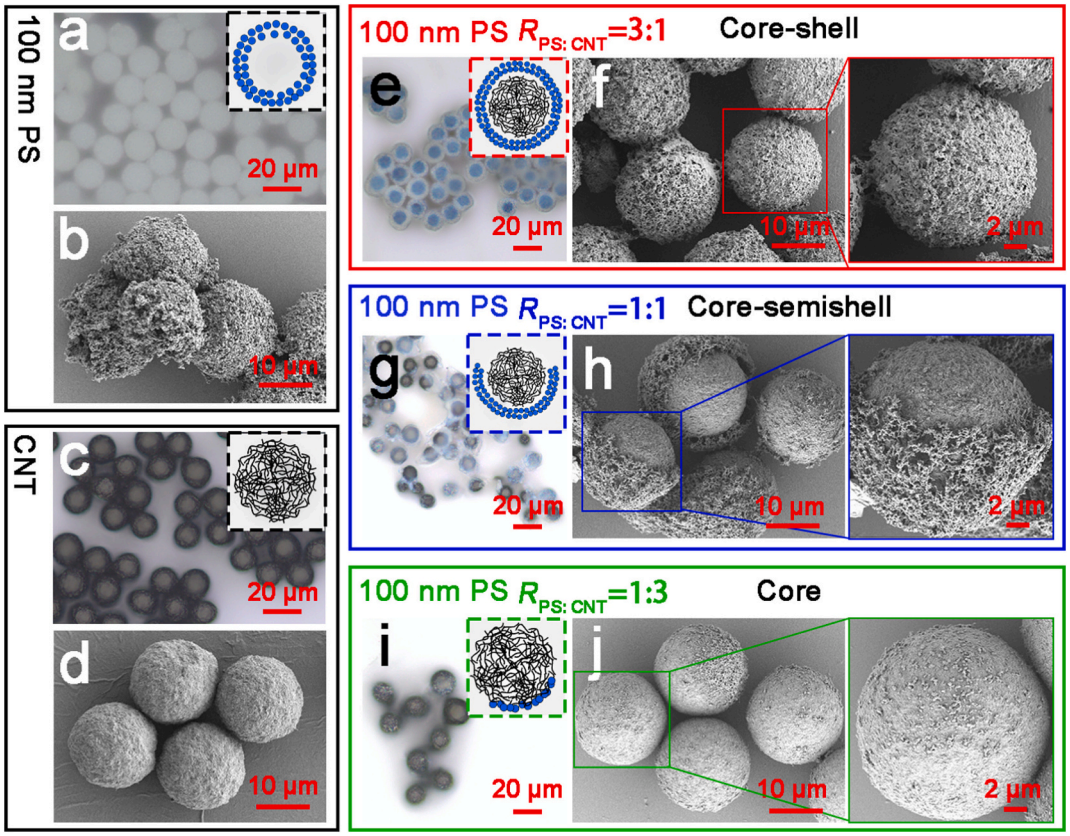

Fig. 2. CNT/PS supraparticles from individualized droplets containing PS (100 nm) and CNT at various mass ratio ($R_{PS:\ CNT}$). (**a**) Optical and (**b**) SEM images of solidified microspheres of single PS (100 nm), and inset is the proposed schematic of PS particle distribution in microsphere. (**c**) Optical and (**d**) SEM images of solidified microspheres of single CNT, and inset is the proposed schematic of CNT distribution in microsphere. (**e**) Optical and (**f**) SEM images of solidified CNT/PS supraparticles with $R_{PS:\ CNT}$ of 3:1, with the inset showing colloidal distribution in the microsphere. (**g**) Optical and (**h**) SEM images of solidified CNT/PS supraparticles with $R_{PS:\ CNT}$ of 1:1, with the inset showing colloidal distribution in the supraparticle. (**i**) Optical and (**j**) SEM images of solidified CNT/PS supraparticles with $R_{PS:\ CNT}$ of 1:3, with the inset showing colloidal distribution in the supraparticle.

simple particle size and ratio.

When d_{PS} = 500 nm, the obtained CNT/PS supraparticle structures differentiated significantly from those with d_{PS} = 100 nm. A microcapsule with loosely packed shell of CNT and PS mixture has been obtained with 500 nm PS particle at an $R_{PS:\ CNT}$ of 3:1, with a representative image shown in Fig. 3a. The green color observed under reflection mode (Fig. 3b) indicates short-range ordering of the 500 nm PS, as depicted in SEM images (Fig. 3c**)**. To validate the shell model, these supraparticles were subjected to thermal treatment (200 °C for 2 h) in an inert atmosphere, leading to the thermal decomposition of PS particles and leaving behind a crumpled shell of CNT, as depicted in Fig. 3d. At an $R_{PS:\ CNT}$ of 1:1, a core-shell microcapsule structure was obtained with a PS shell encapsulating a CNT core (Fig. 3e). Optical reflection images (Fig. 3f) clearly demonstrate the black CNT core, while SEM images (Fig. 3g) present the PS shell. Upon calcination, the supraparticles show a smooth surface formed by entwined CNT (Fig. 3h). When $R_{PS:\ CNT}$ was increased to 1:3, a garnet-like structure formed, with a dense sphere of CNT encapsulating PS particles (Fig. 3i). Optical reflection images suggest the formation of a CNT core (Fig. 3j), while SEM images reveal the exposed PS, indicating the formation of garnet-like structure (Fig. 3k). Subsequent calcination did not change the overall supraparticle morphology, leaving behind pores with corresponding size upon the removal of PS particles (Fig. 3l). SEM images of the fractured supraparticle further confirm the formation of the garnet-like structure (**Fig. S7**).

As a result, the emulsion droplet confined co-assembly of PS and CNT induced to the formation of five types of supraparticle structures, namely core-shell microcapsule, core-shell microparticle, core-semishell microparticle, garnet-like microparticle, and spherical microparticle. The CNT/PS supraparticle structures are correlated with d_{PS} and $R_{PS:\ CNT}$ (Fig. 4a).

The formation of unique structured supraparticles is mainly caused by the microphase segregation of heterogeneous components within the spherical droplet templates, combined with solvent evaporation (**Fig. S8**). Due to the hydrophobicity and high negative potential, PS particles tend to arrange at the oil-water interface, while CNT aggregate to form the core. The microphase segregation occurs faster than solvent evaporation, thus the PS shell initially constructed at the oil-water interface and completely covers the entire spherical interface. If the CNT core is not formed completely or the core is not big enough to fully support the PS shell; as a result, the formed shell may present wrinkles. In addition, if the PS particle is large, for instance 500 nm PS particles, CNT could adsorb onto PS surface to form a stable shell-like structure at $R_{PS:\ CNT}$ = 3:1. While PS is small, for instance 50 nm PS particles, obvious core (CNT) – shell (PS) structure could be obtained at $R_{PS:\ CNT}$ = 3:1.

During the formation of the PS shell, the CNT core can also act as support, preventing deformation of the newly formed PS shell, resulting in well-rounded core-shell structures (as shown in Fig. 4b at $R_{PS\ (500\ nm):\ CNT}$ = 1:1, $R_{PS\ (300\ nm):\ CNT}$ = 3:1, $R_{PS\ (50\ nm):\ CNT}$ = 1:1). With small PS at low content, microphase segregation still occurred to form a semishell of PS due to the relatively limited amount of PS NPs, for instance at $R_{PS\ (50\ nm):\ CNT}$ = 1:3 or $R_{PS\ (100\ nm):\ CNT}$ = 1:1 (Fig. 4b). With large PS at low content, PS NPs were entwined by CNTs and the microphase segregation did not occur, leading to the formation of a garnet-like or spherical microparticle structure at $R_{PS\ (500\ nm):\ CNT}$ = 1:3, or $R_{PS\ (300\ nm):\ CNT}$ = 1:1 (Fig. 4b). Further reduction in PS content would result in the structures similar to single CNT spheres/cores.

3.3. Mechanism of the Core-shell to Core-semishell transformation

Such a CNT/PS supraparticle from droplet confined assembly is influenced by the combined effects of microphase segregation and solvent evaporation, as illustrated in Fig. 4. Therefore, we further explored how the solvent evaporation rate regulated the supraparticles structure, particularly the formation of the semi-shell structure. In the W/O emulsion system, the water inside the droplet could spontaneously form reverse micelles at a high concentration of Span 80 [36,39]. This

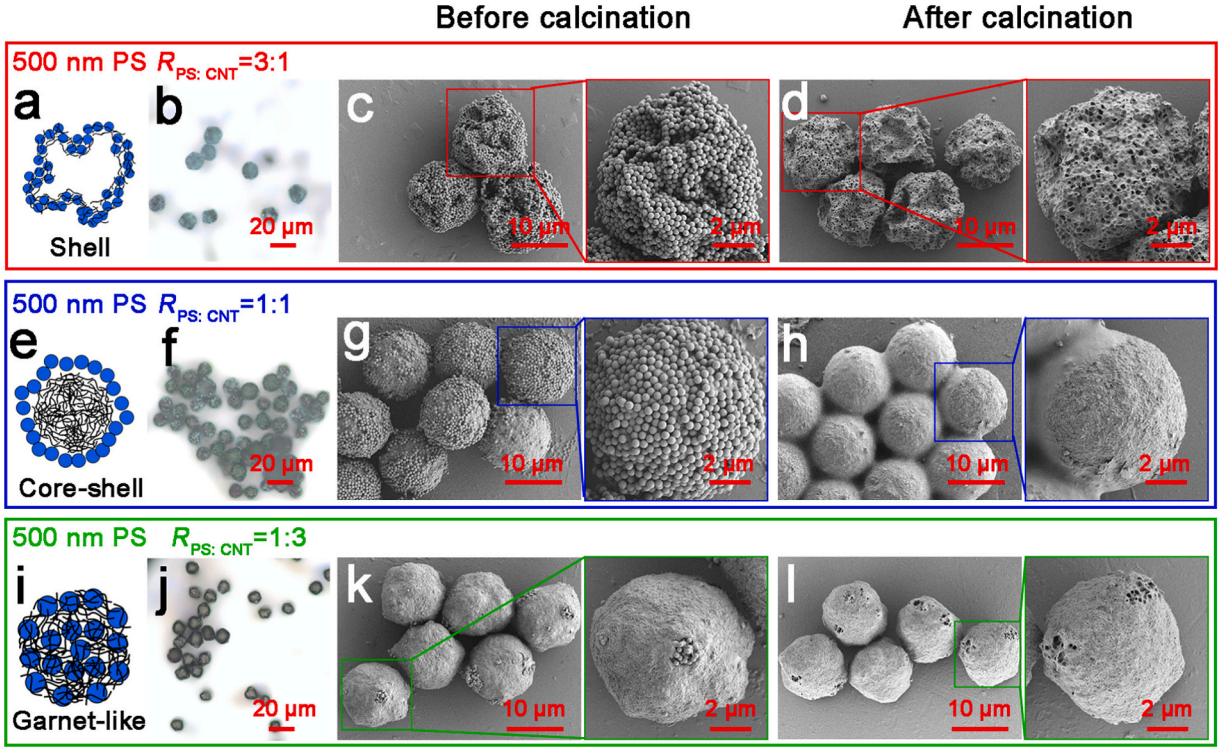

Fig. 3. CNT/PS supraparticles obtained from droplets confined co-assembly of PS (500 nm) and CNT at various $R_{PS:\ CNT}$. (**a**) Schematic drawing and (**b**) optical image of CNT/PS supraparticles suspended in ethanol. SEM images of (**c**) dried and (**d**) calcined CNT/PS supraparticles at $R_{PS:\ CNT}$ of 3:1. (**e**) Schematic drawing and (**f**) optical image of CNT/PS supraparticles suspended in ethanol. SEM images of (**g**) dried and (**h**) calcined CNT/PS supraparticles at $R_{PS:\ CNT}$ of 1:1. (**i**) Schematic drawing and (**j**) optical image of CNT/PS supraparticles suspended in ethanol. SEM images of (**k**) dried and (**l**) calcined CNT/PS supraparticles at $R_{PS:\ CNT}$ of 1:3.

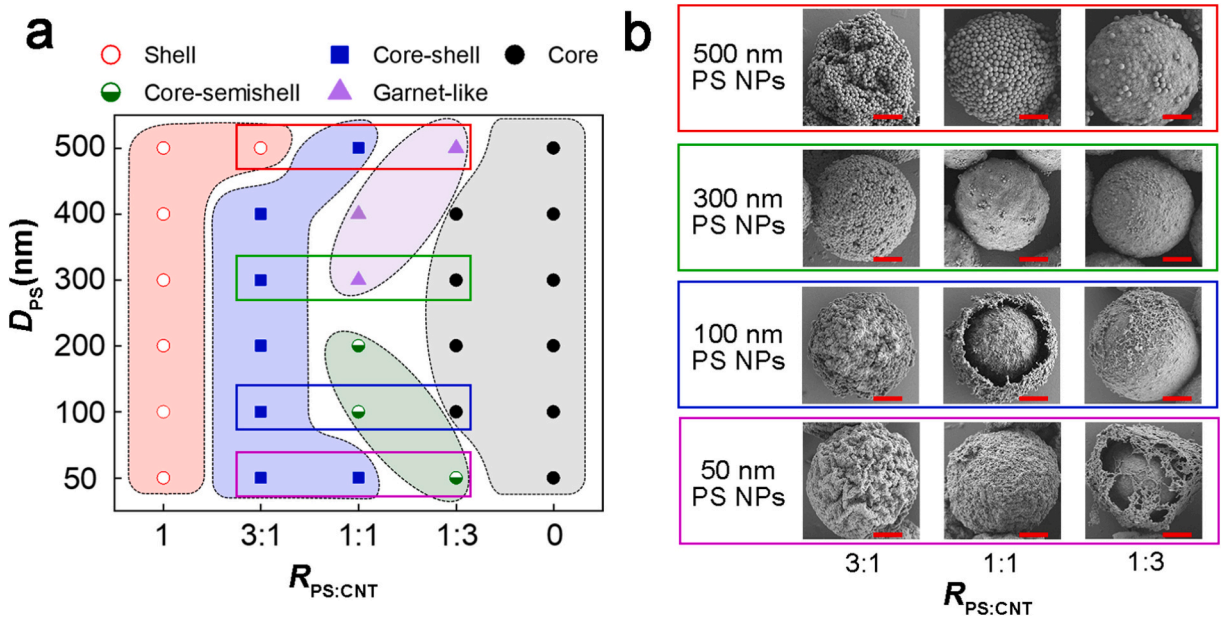

Fig. 4. (**a**) Phase diagram showing the morphology regimes of obtained CNT/PS supraparticles corresponding to d_{PS} and $R_{PS:\ CNT}$. (**b**) SEM images of CNT/PS supraparticles constructed with PS (with various size) and CNT at $R_{PS:\ CNT}$ of 3:1, 1:1 and 3:1 Scale bar in (b) denotes 2 μm.

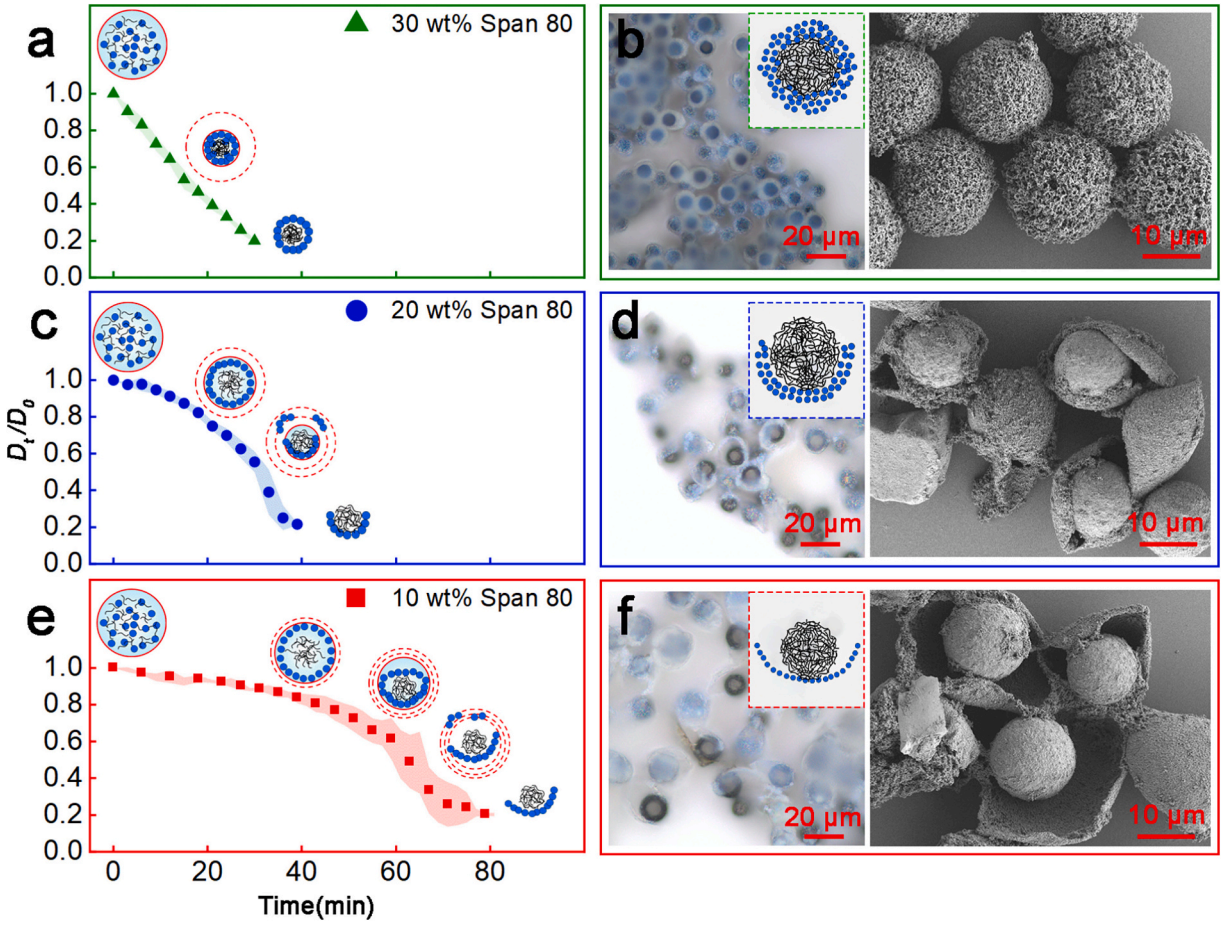

Fig. 5. Influence of Span 80 concentration on the solidification rate and obtained structures of CNT/PS supraparticles. (**a**) Measured shrinkage rate (ratio of the real-time droplet size to the initial droplet size, D_t/D_0) at Span 80 concentration of 30 wt%, and (**b**) optical and SEM images of the corresponding calcined CNT/PS supraparticles obtained at the final stage. (**c**) Measured shrinkage rate at Span 80 concentration of 20 wt%, and (**d**) optical and SEM images of the corresponding calcined CNT/PS supraparticles obtained at the final stage. (**e**) Measured shrinkage rate at Span 80 concentration of 10 wt%, and (**f**) optical and SEM images of the corresponding calcined CNT/PS supraparticles obtained at the final stage. Insets are the schematics of co-assembly process and structures. Here, d_{PS} = 100 nm and $R_{PS:\ CNT}$ = 1:1. Color-striped error bars represent the standard deviation (SD) of shrinkage rates obtained from 50 randomly selected droplets.

emulsification leads to the formation of reverse micelles (water core) that transport water from the droplet into the outer oil medium (**Fig. S4**), where it then diffuses and evaporates. Such a spontaneous emulsification rate of Span 80 reflects the solvent removal rate in droplets, expressed as the ratio of the real-time droplet size (denoted as D_t) to the initial droplet size (denoted as D_0), which is defined as D_t/D_0. The main factors controlling the spontaneous emulsification rate are the Span 80 concentration and the environmental temperature.

The structural transformation of the supraparticles is primarily driven by the rate of water removal, with secondary contribution from the change in the confinement effect due to viscosity change with addition of Span 80. As shown in Fig. 5a, as the mass fraction of Span 80 in the oil phase decreases, the CNT/PS supraparticles evolves from a complete core-shell structure to a closed semi-shell and ultimately to an open semi-shell. At 25 °C, the rate of water transfer and removal gradually decelerates as the Span 80 concentration decrease. This reduction in Span 80 concentration also leads to a decrease in the viscosity of the oil phase (**Fig. S9a**), which weakens the confinement effect [40].

At Span 80 concentration of 30 wt%, it took ~30 min for droplets to dry into supraparticles. As shown in Fig. 5a and **Fig. S10a**, a thick PS shell formed at D_t/D_0 of ~0.6 at 18 min and fully encapsulating the CNT core, namely core-shell CNT/PS supraparticles (Fig. 5b). As the Span 80 concentration decreased to 20 wt%, the drying time increases to ~40 mins (Fig. 5c). A thin PS shell formed at 25 min with D_t/D_0 of ~0.7, and the CNT core formed at 30 min with D_t/D_0 of ~0.6. The thin PS shell disrupts and shrinks into a semi-shell due to the solvent removal and the formation of CNT core (**Fig. S10b**), inducing the formation of a closed core-semishell CNT/PS supraparticles (Fig. 5d). When the Span 80

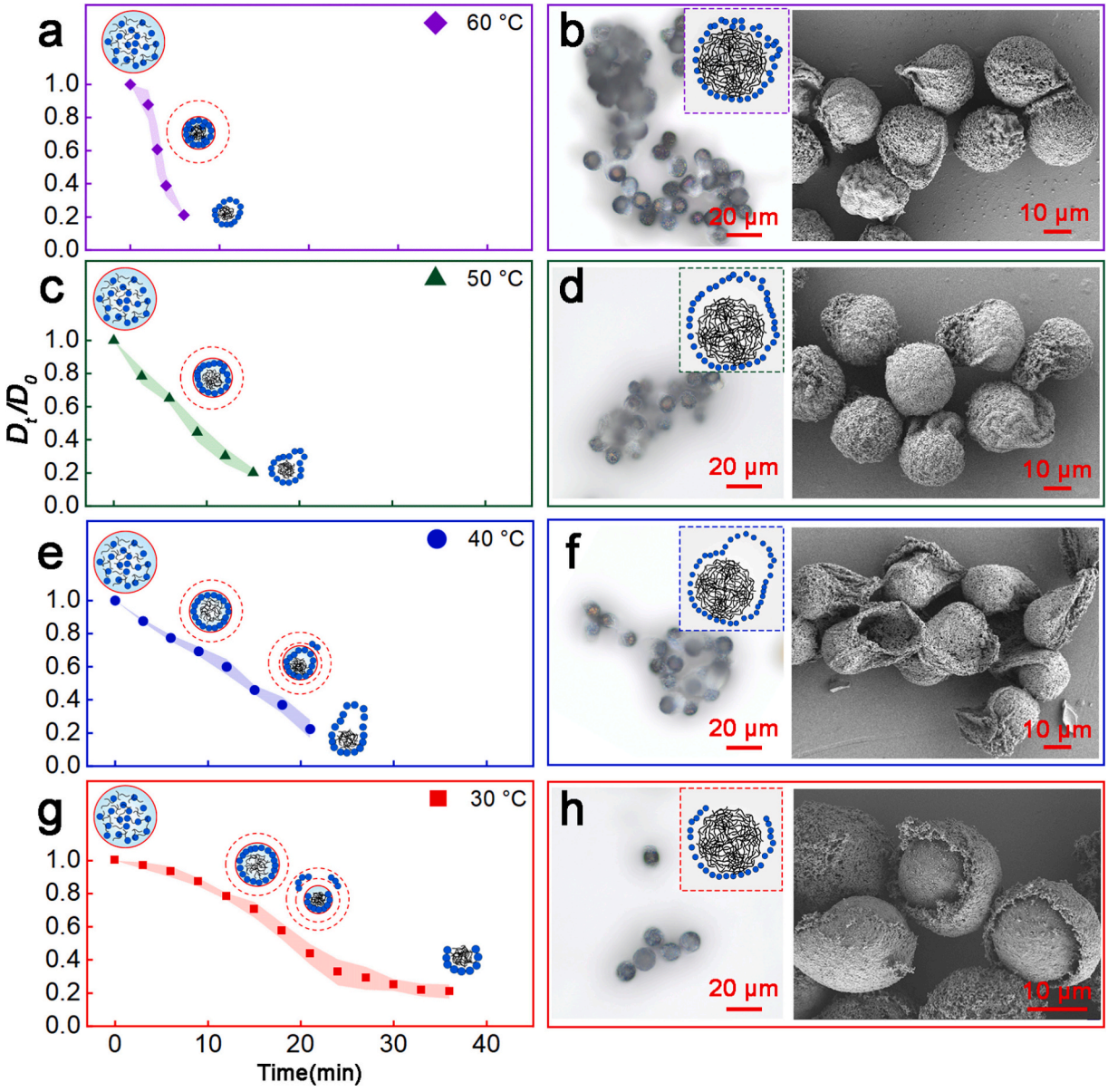

Fig. 6. Influence of drying temperature on the solidification rate and obtained structures of CNT/PS supraparticles. (**a**) Measured shrinkage rate (D_t/D_0) at drying temperature of 60 °C, and (**b**) optical and SEM images of the corresponding calcined CNT/PS supraparticles obtained at the final stage. (**c**) Measured shrinkage rate at drying temperature of 50 °C, and (**d**) optical and SEM images of the corresponding calcined CNT/PS supraparticles obtained at the final stage. (**e**) Measured shrinkage rate at drying temperature of 40 °C, and (**f**) optical and SEM images of the corresponding calcined CNT/PS supraparticles obtained at the final stage. (**g**) Measured shrinkage rate at drying temperature of 30 °C, and (**h**) optical and SEM images of the corresponding calcined CNT/PS supraparticles obtained at the final stage. Insets are the schematics of co-assembly process and structures. Here, d_{PS} = 100 nm and $R_{PS:\ CNT}$ = 1:1. Color-striped error bars represent the standard deviation (SD) of shrinkage rates obtained from 50 randomly selected droplets.

concentration further decreases to 10 wt%, the drying time increases to ~80 min (Fig. 5e). A flexible and thin PS shell formed at 40 min with D_t/D_0 of 0.8, and the CNT core formed at 60 min with D_t/D_0 of ~0.7. The PS shell deformed and eventually broke as solvent is removed, allowing the formation of a CNT core open semi-shell structure (**Fig. S10c** and Fig. 5f).

The structural changes in CNT/PS supraparticles induced by drying temperature variations confirm the significant role of solvent removal in regulating assembly structures. As depicted in Fig. 6a, when using the hexadecane containing 20 wt% Span 80 as the outer oil phase, the time required for droplets to dry into supraparticles was approximately 8 min at 60 °C. Similar to the behavior observed with 30 wt% Span 80 hexadecane oil phase, a PS shell formed at 5 min with D_t/D_0 of ~0.7, completely encapsulating the CNT core. With increasing temperature, the oil phase viscosity decreased, weakening the confinement effect (**Fig. S9b**). Consequently, even at 60 °C, where the evaporation rate is sufficient to form a complete core-shell structure (**Fig. S11a**), the diminishing confinement effect leads to the deformation of PS shell (Fig. 6b).

At a drying temperature of 50 °C, the drying time increased to ~18 min (Fig. 6c). The PS shell formed at 10 min with D_t/D_0 of 0.6, followed by the formation of the CNT core (**Fig. S11b**). Although the CNT/PS supraparticles still retained a core-shell structure, the delayed formation of the PS shell led to increased deformation (Fig. 6d). When the drying temperature was decreased further to 40 °C, it took approximately 22 min to form the supraparticles. As shown in Fig. 6e and **Fig. S11c**, the PS shell formed at ~10 min with D_t/D_0 of ~0.6, while the CNT core formed at ~18 min with D_t/D_0 of ~0.4. As a result, the significant deformation of the PS shell induced the emergence of the core-semishell structure (Fig. 6f). At a drying temperature of 30 °C, the drying time increased to 35 min (Fig. 6g). The thin PS shell formed at ~15 min with D_t/D_0 of ~0.7 (**Fig. S11d**), with the formation of the CNT core at ~20 min with

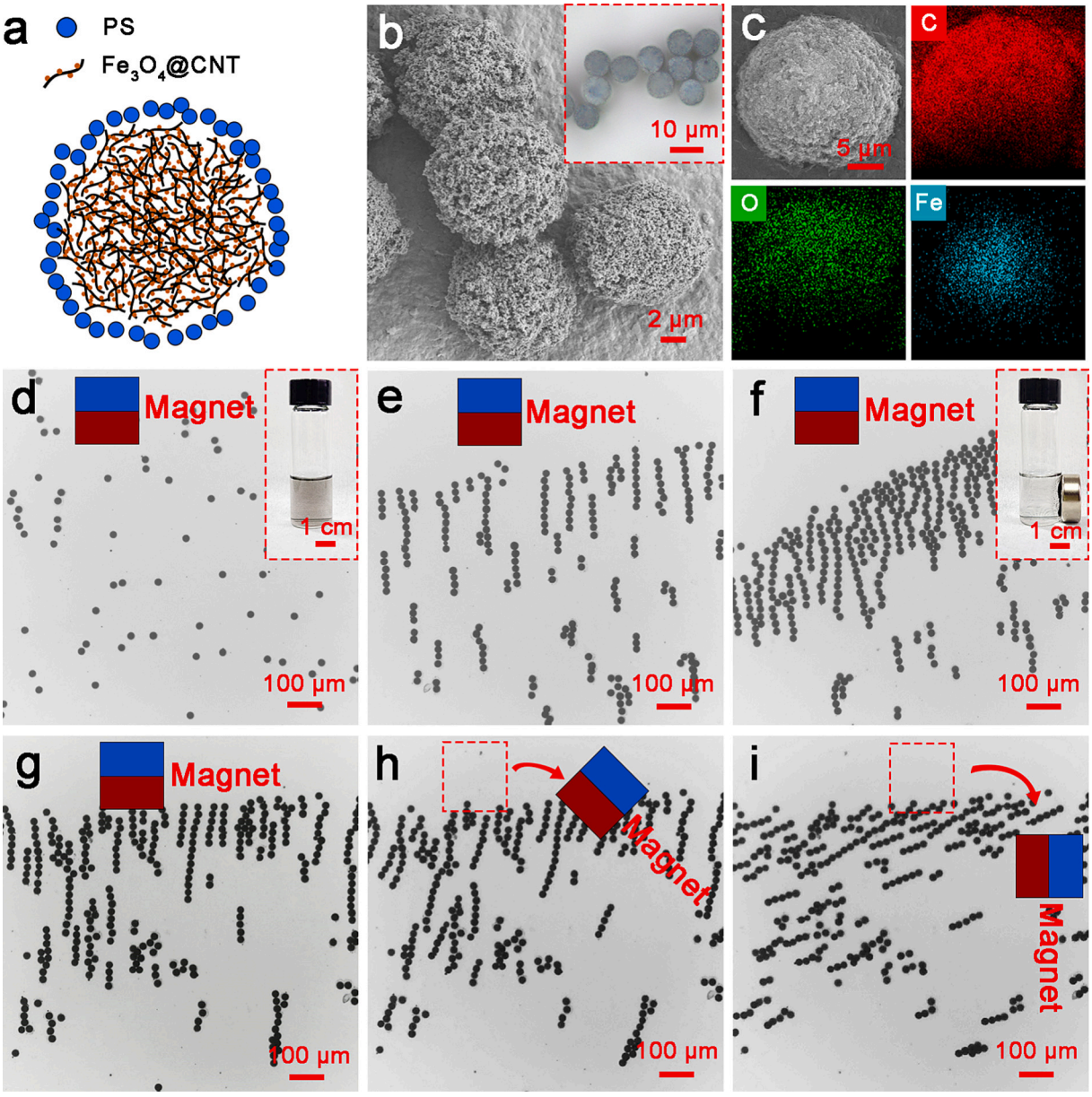

Fig. 7. (**a**) Schematic drawing of the core-shell PS/Fe_3O_4@CNT supraparticles. (**b**) SEM image of core-shell PS/Fe_3O_4@CNT supraparticles, with the inset for its optical image. (**c**) EDS elemental mapping of carbon (C), oxygen (O) and iron (Fe) on the supraparticle. (**d-f**) PS/Fe_3O_4@CNT supraparticles moved and aligned corresponding to the static magnet position and orientation. The inset in (**d**) is the photo of supraparticles suspension, and the inset in (**f**) shows the collection of supraparticles via magnetic force. (**g-i**) PS/Fe_3O_4@CNT supraparticles form chains and rotate with the magnetic orientation.

D_t/D_0 of ~0.5, the shell shrank into a semi-shell (Fig. 6h). The structural transition from core-shell to core-semishell was highly reproducible across five independent experiments (Fig. 6g-h, **S12**). The critical D_t/D_0 values for PS shell formation of 0.7 ± 0.1 and for CNT core stabilization of 0.5 ± 0.1 confirm that the formed structures are governed by controllable parameters rather than stochastic effects.

Through systematic manipulation of both surfactant concentration and drying temperature, we have successfully modulated the structures of CNT/PS supraparticles, revealing a deformation mechanism from core-shell to core-semishell configurations. The structural regulation of binary colloidal supraparticles can be achieved by adjusting the composition and properties of the internal components, as well as by tuning the experimental parameters. This method opens up a promising path for the design and construction of multi-component supraparticles, catering to the growing demand for high-performance material.

3.4. Hybrid Magnetic CNT@Fe_3O_4/PS Supraparticles

To validate the effectiveness of the proposed strategy for preparing supraparticles with conferrable functionality, we employed CNT@Fe_3O_4 as the core material (**Fig. S13**). Utilizing the flow-focusing microfluidic device, the magnetic core-shell CNT@Fe_3O_4/PS supraparticles were successfully constructed, as illustrated in Fig. 7a. Here, a hexadecane solution containing 20 wt% Span 80 worked as the outer phase while the inner phase was an aqueous dispersion containing PS (100 nm) and CNT@Fe_3O_4 with a mass ratio of 1:1. The drying temperature was controlled at 25 °C. The core-semishell magnetic supraparticles was obtained at a mass ratio of PS to CNT@Fe_3O_4 of 1:3 (**Fig. S14**).

The SEM image and optical images confirmed the successful construction of both core-shell CNT@Fe_3O_4/PS supraparticles (Fig. 7b) and core-semishell CNT@Fe_3O_4/PS supraparticles (**Fig. S14b**). SEM elemental mapping (Fig. 7c **and Fig. S14c**) confirmed the supraparticle structure including a PS shell and a magnetic CNT@Fe_3O_4 core. The diameter of the core-shell CNT@Fe_3O_4/PS supraparticles was 10 ± 1 μm. In the flow-focusing microfluidic device, microdroplets were generated at a frequency of about 1 kHz.

The flow-focusing microfluidic device demonstrates a strategic balance between precision and scalability when benchmarked against conventional methods. **Table S1** summarizes the current methods for supraparticle production, including spray drying, emulsion-based methods, the superhydrophobic surface-mediated method, and microfluidics. Each of these methods exhibits a distinct trade-off between output and precision. Spray-drying, while offering high output (10–1000 g/h), typically yields particles with high polydisperse (CV > 15 %) with limited control over internal structures [41]. Stirring emulsification achieves moderate output (1–10 g/h) but lacks structural precision [42]. In contrast, the superhydrophobic surface-mediated method enables fine structural tuning, yet its scalability is constrained by the reliance on specialized substrates [13]. Microfluidic technology combines both structural precision and scalable output. Although the current output is lower than spray-drying, microfluidics eliminates material waste and enables complex compositions inaccessible to bulk methods. And the output can be scaled up via channel/capillary parallelization without sacrificing uniformity, suggesting microfluidics as a versatile platform for high-precision supraparticle design where quality outweighs sheer production volume.

The core-shell CNT@Fe_3O_4/PS supraparticles were stably dispersed in neutral aqueous solutions, ethanol or hexadecane. As shown in Fig. 7d-f, the CNT@Fe_3O_4/PS supraparticles dispersed in hexadecane, aligned and formed chains along the field's direction when subjected to a stationary magnetic field. Upon altering the magnetic field orientation, the supraparticle chains rotated accordingly (Fig. 7g-i). Such core-shell CNT@Fe_3O_4/PS supraparticles demonstrated significant magnetic responsiveness, allowing them to be effectively separated using magnetic field during the recycling process. By applying a magnet, we were able to easily attract and separate the supraparticles, facilitating further processing and recycling, as illustrated in the insets of Fig. 7d and Fig. 7f. It is noted that the micrometric scale supraparticles were visible under normal microscopy and could stay stably without agglomeration, exhibiting the potential for analytical and biomedical applications [43]. In addition, the core and shell materials and supraparticle size could be tuned based on practical demands.

To systematically investigate the structure-property relationship in magnetic supraparticles, we conducted a comparative analysis of the supraparticles with core-shell ($R_{PS:CNT@Fe_3O_4}$ = 1:1) and core-semishell ($R_{PS:CNT@Fe_3O_4}$ = 1:3) architectures (**Fig. S15**). Both supraparticles exhibited characteristic superparamagnetic behavior, with the core-shell structure demonstrating a saturation magnetization of 3.2 emu/g compared to 3.7 emu/g for the core-semishell variant. This difference might be attributed to the content variation of magnetic components in the core-semishell supraparticles. Notably, despite its slightly low saturation magnetization value, the core-shell architecture displayed superior performance in field-directed applications (Fig. 7d-i). This advantage stems from two structural features of the symmetrical architecture enabling efficient alignment under external magnetic fields and the complete PS shell providing enhanced stability during repeated magnetization cycles. Combined with microfluidic technology, monodisperse droplet template preparation was achieved, ensuring the controllable and reproducible production of the supraparticles. This approach not only expands the application scope of microfluidic technology but also provides a new pathway for material design and practical application, particularly facilitating the application of nano- and micro- materials in macroscopic scenarios [44].

4. Conclusion

In summary, we demonstrate a droplet confined co-assembly strategy to fabricate hierarchical CNT/PS hybrid supraparticles with precisely tunable architectures (core-shell microcapsule, core-shell microsphere, core-semishell microsphere, garnet-like microsphere and densely packed microsphere). The droplet-based microfluidic technology allowed the preparation of monodisperse droplet templates with tunable size and composition. The architectures of the formed supraparticles are governed by a dynamic balance among the colloidal particles of PS and CNT, their mass ratio and the PS size. A factor of solvent removal kinetics was found to play a critical role for the formation of different architectures. By correlating the reversed micelle formation according to Span 80 and the phase separation from the solvent evaporation and temperature, we revealed a new pathway to modulate water removal speed, enabling structural transitions (e.g., core-shell to core-semishell) for the droplet confined co-assembly of binary colloidal particles. The successful integration of Fe_3O_4 nanoparticles to create magnetic-responsive CNT@Fe_3O_4/PS supraparticles underscores the method's versatility for multifunctional hybrid design. The tunable porosity and CNT network topology of these supraparticles hold promise for macroscopic applications, such as magnetic-responsive microrobots and lightweight conductive foams (CNT-rich cores) for flexible electronics. These findings bridge the nanoscale-to-macroscopic gap by translating colloidal-scale control into bulk material properties.

CRediT authorship contribution statement

Huan Liu: Writing – review & editing, Writing – original draft, Visualization, Validation, Supervision, Resources, Project administration, Methodology, Investigation, Formal analysis, Data curation, Conceptualization. **Shijian Huang:** Writing – review & editing, Writing – original draft, Visualization, Validation, Supervision, Methodology, Investigation, Formal analysis, Data curation, Conceptualization. **Zhenping Liu:** Writing – review & editing, Visualization, Supervision, Resources. **Lang Chen:** Resources, Methodology, Investigation. **Jiamei Chen:** Writing – review & editing, Visualization. **Xinyi Li:** Methodology, Investigation, Data curation. **Mengjun Liu:** Writing – review & editing.

Haoqiang Feng: Writing – review & editing, Visualization. **Weilong Xu:** Investigation. **Ruizhi Yang:** Writing – review & editing, Validation, Methodology. **Minmin Zhang:** Writing – review & editing. **Lingling Shui:** Writing – review & editing, Supervision, Resources, Funding acquisition, Formal analysis, Data curation, Conceptualization.

Declaration of generative AI and AI-assisted technologies in the writing process

During the preparation of this work the authors used OpenAI in order to improve language and readability. After using this tool, the authors reviewed and edited the content as needed and take full responsibility for the content of the publication.

Declaration of competing interest

The authors declare that they have no known competing financial interests or personal relationships that could have appeared to influence the work reported in this paper.

Acknowledgements

We acknowledge the financial support from the National Natural Science Foundation of China (No. 12372262, No. 12131010, No. 22402062), the Guangdong Province Basic and Applied Basic Research Foundation (No. 2023A1515012471, No. 2025A1515012964), Scientific Research Innovation Project of Graduate School of South China Normal University and Special Funds for the Cultivation of Guangdong College Students' Scientific and Technological Innovation. ("Climbing Program" Special Funds: pdjh2024a111).

Appendix A. Supplementary data

Supplementary data to this article can be found online at https://doi.org/10.1016/j.jcis.2025.138344.

Data availability

All data needed to evaluate the conclusions in the paper are present in the paper and/or the Supplementary Materials. The data that support the findings of this study are available from the corresponding author upon reasonable request.

References

[1] S. Wintzheimer, T. Granath, M. Oppmann, T. Kister, T. Thai, T. Kraus, N. Vogel, K. Mandel, Supraparticles: functionality from uniform structural motifs, ACS Nano 12 (6) (2018) 5093–5120.
[2] X. Wang, Y. Lian, S. Xiang, S. Tao, M. Kappl, W. Liu, Droplet evaporation on super liquid-repellent surfaces: a controllable approach for supraparticle fabrication, Adv. Colloid Interface Sci. 334 (2024) 103305.
[3] C.L. Bassani, G. van Anders, U. Banin, D. Baranov, Q. Chen, M. Dijkstra, M. S. Dimitriyev, E. Efrati, J. Faraudo, O. Gang, N. Gaston, R. Golestanian, G. I. Guerrero-Garcia, M. Gruenwald, A. Haji-Akbari, M. Ibáñez, M. Karg, T. Kraus, B. Lee, R.C. Van Lehn, R.J. Macfarlane, B.M. Mognetti, A. Nikoubashman, S. Osat, O.V. Prezhdo, G.M. Rotskoff, L. Saiz, A.-C. Shi, S. Skrabalak, I.I. Smalyukh, M. Tagliazucchi, D.V. Talapin, A.V. Tkachenko, S. Tretiak, D. Vaknin, A. Widmer-Cooper, G.C.L. Wong, X. Ye, S. Zhou, E. Rabani, M. Engel, A. Travesset, Nanocrystal assemblies: current advances and open problems, ACS Nano 18 (23) (2024) 14791–14840.
[4] V.D. Ta, T.V. Nguyen, T.A. Doan, D.C. Duong, S. Caixeiro, D. Saxena, R. Sapienza, Random lasing in micron-sized individual supraparticles, Opt. Lett. 49 (14) (2024) 3886–3889.
[5] J. Cao, Y. Huang, Z. Shang, X. Liu, C. Lu, H. Chen, P. Liang, G. Ma, Fabrication of core shell Au@Ag supraparticles with 3D hotspots via evaporation self-assembly for sensitive surface enhanced Raman scattering detection, Sens. Actuators B 382 (2023) 133529.
[6] J.E.S. van der Hoeven, H. Gurunarayanan, M. Bransen, D.A.M. de Winter, P.E. de Jongh, A. van Blaaderen, Silica-coated gold nanorod supraparticles: a tunable platform for surface enhanced Raman spectroscopy, Adv. Funct. Mater. 32 (27) (2022) 2200148.
[7] J. Reichstein, P. Groppe, N. Stockinger, C. Cuadrado Collados, M. Thommes, S. Wintzheimer, K. Mandel, Safety through visibility: tracing hydrogen in colors with highly customizable and flexibly applicable Supraparticle additives, Advanced Materials Technologies 9 (17) (2024) 2400441.
[8] J. Reichstein, L. Luthardt, V.G. Martello, A. Pianetti, S. Wintzheimer, K. Mandel, Modulating the microenvironment of coumarin dyes within multihierarchical Supraparticles: En route toward versatile luminescent dual-threshold temperature indicators with ratiometric readout, Advanced Optical Materials 12 (18) (2024) 2303346.
[9] P. Groppe, J. Reichstein, S. Carl, C. Cuadrado Collados, B.-J. Niebuur, K. Zhang, B. Apeleo Zubiri, J. Libuda, T. Kraus, T. Retzer, M. Thommes, E. Spiecker, S. Wintzheimer, K. Mandel, Catalyst supraparticles: tuning the structure of spray-dried Pt/SiO_2 supraparticles via salt-based colloidal manipulation to control their catalytic performance, Small 20 (35) (2024) 2310813.
[10] K. Hou, J. Han, Z. Tang, Formation of supraparticles and their application in catalysis, ACS Materials Letters 2 (1) (2020) 95–106.
[11] X. Wu, A. Chen, X. Yu, Z. Tian, H. Li, Y. Jiang, J. Xu, Microfluidic synthesis of multifunctional micro-/nanomaterials from process intensification: structural engineering to high electrochemical energy storage, ACS Nano 18 (32) (2024) 20957–20979.
[12] S.L. Deuso, S. Ziegler, D. Weber, F. Breuer, D. Haddad, S. Müssig, A. Flegler, G. A. Giffin, K. Mandel, Magnetic supraparticles as identifiers in single-layer lithium-ion battery pouch cells, ChemSusChem 18 (6) (2025) e202401142.
[13] W. Liu, M. Kappl, W. Steffen, H.-J. Butt, Controlling supraparticle shape and structure by tuning colloidal interactions, J. Colloid Interface Sci. 607 (2022) 1661–1670.
[14] H. Tan, S. Wooh, H.-J. Butt, X. Zhang, D. Lohse, Porous supraparticle assembly through self-lubricating evaporating colloidal ouzo drops, Nat. Commun. 10 (1) (2019) 478.
[15] J. Wang, S. Hahn, E. Amstad, N. Vogel, Tailored double emulsions made simple, Adv. Mater. 34 (5) (2022) 2107338.
[16] Y.H. Choi, J. Lee, E. Amstad, S.-H. Kim, Influence of sphericity on surface termination of icosahedral colloidal clusters, Small 20 (20) (2024) 2309512.
[17] P.M. Naveenkumar, L.J. Roemling, U. Sultan, N. Vogel, Fabrication of spherical colloidal supraparticles via membrane emulsification, Langmuir 40 (42) (2024) 22245–22255.
[18] S. Huang, J. Yao, X. Li, H. Liu, Y. Qin, X. Wang, D. Luo, L. Shui, Tuning size and composition of Si/CNT composite microspheres via droplet-microfluidics for high performance lithium-ion batteries, APL Mater. 12 (1) (2024) 011126.
[19] H. Feng, S. Shen, M. Jin, M. Xiao, M. Liu, Q. Zhang, H. Jiang, Z. Yi, W. Wu, G. Zhou, L. Shui, Massive electro-microfluidic particle assembly patterns in droplet array for information encoding, Small 20 (48) (2024) 2405161.
[20] S. Shen, H. Feng, Y. Deng, S. Xie, Z. Yi, M. Jin, G. Zhou, P. Mulvaney, L. Shui, A reflective display based on the electro-microfluidic assembly of particles within suppressed water-in-oil droplet array, Light: Science & Applications 12 (1) (2023) 290.
[21] N. Yan, Y. Song, Y. Zhu, Confined self-assembly of block copolymers in emulsion droplets: preparation, shape and internal structure, and applications, J. Polym. Sci. 61 (24) (2023) 3211–3227.
[22] J. Wang, E. Kang, U. Sultan, B. Merle, A. Inayat, B. Graczykowski, G. Fytas, N. Vogel, Influence of surfactant-mediated interparticle contacts on the mechanical stability of supraparticles, J. Phys. Chem. C 125 (42) (2021) 23445–23456.
[23] X. Ma, L. Ma, Y. Tan, X. Chen, Q. Tong, L. Tang, X. Cao, D. Liu, X. Li, Biomimetic mineralization by confined diffusion with viscous hyaluronan network: assembly of hierarchical flower-like supraparticles, Carbohydr. Polym. 322 (2023) 121345.
[24] W. Liu, M. Kappl, H.-J. Butt, Tuning the porosity of supraparticles, ACS Nano 13 (12) (2019) 13949–13956.
[25] K. Chen, S. Schünemann, H. Tüysüz, Preparation of waterproof organometal halide perovskite photonic crystal beads, Angew. Chem. Int. Ed. 56 (23) (2017) 6548–6552.
[26] Z. Hu, H. Sun, M.P. Thompson, M. Xiao, M.C. Allen, X. Zhou, Q.Z. Ni, Z. Wang, W. Li, M.D. Burkart, D.D. Deheyn, A. Dhinojwala, M.D. Shawkey, N.C. Gianneschi, Structurally colored inks from synthetic melanin-based crosslinked Supraparticles, ACS Materials Letters 3 (1) (2021) 50–55.
[27] B. de Nijs, S. Dussi, F. Smallenburg, J.D. Meeldijk, D.J. Groenendijk, L. Filion, A. Imhof, A. van Blaaderen, M. Dijkstra, Entropy-driven formation of large icosahedral colloidal clusters by spherical confinement, Nat. Mater. 14 (1) (2015) 56–60.
[28] J. Wang, Y. Liu, G. Bleyer, E.S.A. Goerlitzer, S. Englisch, T. Przybilla, C.F. Mbah, M. Engel, E. Spiecker, I. Imaz, D. Maspoch, N. Vogel, Coloration in supraparticles assembled from polyhedral metal-organic framework particles, Angew. Chem. Int. Ed. 61 (16) (2022) e202117455.
[29] B. Jiang, J. Zhang, K. Yu, Z. Jia, H. Long, N. He, Y. Zhang, Y. Zou, Z. Han, Y. Li, L. Ma, Dynamic cleavage-remodeling of covalent organic networks into multidimensional superstructures, Adv. Mater. 36 (32) (2024) 2404446.
[30] D. Wang, M. Hermes, S. Najmr, N. Tasios, A. Grau-Carbonell, Y. Liu, S. Bals, M. Dijkstra, C.B. Murray, A. van Blaaderen, Structural diversity in three-dimensional self-assembly of nanoplatelets by spherical confinement, Nat. Commun. 13 (1) (2022) 6001.
[31] T. Zimmermann, N. Madubuko, P. Groppe, T. Raczka, N. Dünninger, N. Taccardi, S. Carl, B. Apeleo Zubiri, E. Spiecker, P. Wasserscheid, K. Mandel, M. Haumann, S. Wintzheimer, Supraparticles on beads for supported catalytically active liquid metal solutions – the SCALMS suprabead concept, Mater. Horiz. 10 (11) (2023) 4960–4967.
[32] K. Zhang, J. Reichstein, P. Groppe, S. Schoetz, N. Stockinger, J. Libuda, K. Mandel, S. Wintzheimer, T. Retzer, Molecular and structural insights into H_2 indicator

supraparticles: lowering the limit of detection by tuning incorporated catalyst nanoparticles, Chem. Mater. 35 (17) (2023) 6808–6822.
[33] J. Yao, Z. Liu, M. Jin, Y. Zou, J. Chen, P. Xie, X. Wang, E.M. Akinoglu, G. Zhou, L. Shui, Uniform honeycomb CNT-microparticles prepared via droplet-microfluidics and sacrificial nanoparticles for electrochemical determination of methyl parathion, Sens. Actuators B 321 (2020) 128517.
[34] Z. Wang, L. Wu, J. Zhou, W. Cai, B. Shen, Z. Jiang, Magnetite nanocrystals on multiwalled carbon nanotubes as a synergistic microwave absorber, J. Phys. Chem. C 117 (10) (2013) 5446–5452.
[35] D. Copic, L. Maggini, M. De Volder, Monodisperse CNT microspheres for high permeability and efficiency flow-through filtration applications, Adv. Mater. 30 (12) (2018) 1706503.
[36] K.A. Sanders, M.F.L. De Volder, Controlled fabrication of carbon nanotube microspheres from emulsion templates: exploring the dynamics of solvent loss and nanoparticle assembly, Adv. Mater. Interfaces 10 (1) (2023) 2201728.
[37] V.I. Uricanu, M.H.G. Duits, D. Filip, R.M.F. Nelissen, W.G.M. Agterof, Surfactant-mediated water transport at gelatin gel/oil interfaces, J. Colloid Interface Sci. 298 (2) (2006) 920–934.
[38] C. Wu, Q. Fan, Y. Yin, Emulsion-confined self-assembly of colloidal nanoparticles into 3D superstructures, Cell Reports Physical Science 3 (12) (2022) 101162.
[39] M. Schmitt, R. Toor, R. Denoyel, M. Antoni, Spontaneous microstructure formation at water/paraffin oil interfaces, Langmuir 33 (49) (2017) 14011–14019.
[40] G. Guo, L. Ji, X. Shen, B. Wang, H. Li, J. Hu, D. Yang, A. Dong, Self-assembly of transition-metal-oxide nanoparticle supraparticles with designed architectures and their enhanced lithium storage properties, J. Mater. Chem. A 4 (41) (2016) 16128–16135.
[41] A. Wolf, H. Zhou, P. Groppe, L.M.S. Stiegler, T. Kämäräinen, W. Peukert, J. Walter, S. Wintzheimer, K. Mandel, Nanoparticle clustering in Supraparticles to control magnetic Long-range interactions, Part. Part. Syst. Charact. 42 (3) (2025) 2400180.
[42] C. Kim, K. Jung, J.W. Yu, S. Park, S.-H. Kim, W.B. Lee, H. Hwang, V.N. Manoharan, J.H. Moon, Controlled assembly of icosahedral colloidal clusters for structural coloration, Chem. Mater. 32 (22) (2020) 9704–9712.
[43] S. Wintzheimer, J. Reichstein, P. Groppe, A. Wolf, B. Fett, H. Zhou, R. Pujales-Paradela, F. Miller, S. Müssig, S. Wenderoth, K. Mandel, Supraparticles for sustainability, Adv. Funct. Mater. 31 (11) (2021) 2011089.
[44] J. Reichstein, S. Müssig, S. Wintzheimer, K. Mandel, Communicating supraparticles to enable perceptual, information-providing matter, Adv. Mater. 35 (49) (2023) 2306728.